Energy Storage Materials 26 (2020) 543–549

Contents lists available at ScienceDirect

Energy Storage Materials

journal homepage: www.elsevier.com/locate/ensm

Crystallization of *closo*-borate electrolytes from solution enabling infiltration into slurry-casted porous electrodes for all-solid-state batteries

Léo Duchêne [a,b,1], Dong Hyeon Kim [c,1], Yong Bae Song [c], Seunggoo Jun [c], Romain Moury [b,d], Arndt Remhof [a,*], Hans Hagemann [b], Yoon Seok Jung [c,**], Corsin Battaglia [a]

[a] Empa, Swiss Federal Laboratories for Materials Science and Technology, 8600, Dübendorf, Switzerland
[b] Département de Chimie-Physique, Université de Genève, 1211, Geneva 4, Switzerland
[c] Department of Energy Engineering, Hanyang University, 04763, Seoul, Republic of Korea
[d] Institut des Molécules et Matériaux Du Mans, Le Mans Université, 72085, Le Mans, France

ARTICLE INFO

Keywords:
Solid state battery
Full cell
Hydroborate
Infiltration process

ABSTRACT

The direct crystallization of a *closo*-borate solid electrolyte from solution is demonstrated and applied to infiltrate porous battery electrodes fabricated by traditional slurry casting methods. Employing isopropanol as a solvent, we show that $Na_4(B_{12}H_{12})(B_{10}H_{10})$ crystallizes inside the open porosity of the electrodes with the appropriate crystal structure yielding high ionic conductivity (1 mS cm^{-1} at 25 °C) and providing efficient contact to the active materials. Very stable cycling is demonstrated at 30 °C for $NaCrO_2$|Na-Sn half cells employing infiltrated $NaCrO_2$ cathodes with mass loadings of ~7.7 mg cm^{-2} at rates up to 5C (4.5 mA cm^{-2}). The all-solid-state cells exhibit remarkable cycling stability at moderate (70 MPa), and low (3 MPa) applied external pressure, retaining 95.6% and 85.9% of the initial capacity after 100 cycles at 0.5C respectively. A $NaCrO_2$|Sn rocking-chair all-solid-state full cell with capacity-balanced infiltrated electrodes is also demonstrated. The more pronounced fading of the full cell is characterized with a three-electrode measurement and can be attributed to the poorer cyclability of Sn. This work bridges the gap between the attractive materials properties of *closo*-borate electrolytes and their integration into all-solid-state batteries facilitating their adoption in industrial cell production at scale.

1. Introduction

Lithium-ion batteries have become ubiquitous as power sources for portable electronics, and their application is extended to the growing electric mobility market. Given their widespread deployment, fabrication protocols for their components are well established in industry. In parallel, intense research efforts are currently directed to the development of all-solid-state batteries (ASSBs), aiming to replace the flammable organic liquid electrolyte in today's lithium-ion batteries with a solid ion conductor for improved safety, and increased energy and power density [1,2]. Furthermore, the development of sodium-ion-conducting solid electrolytes could be desired for potentially more cost-effective sodium-based batteries [3].

Significant progress has been made in finding candidate solid electrolytes that fulfill the criteria of high ionic conductivity and high (electro-)chemical stability for ASSBs [4–7]. On the way to commercialization, criteria related to their processing into cells become equally important as fabrication protocols will strongly depend on the class of material chosen as the solid electrolyte [8,9]. While oxide-ceramic electrolytes require high-temperature sintering to establish ionic contact between grains, sulfide-based electrolytes can be processed at room temperature owing to their high deformability and may be prepared from solution [2,8,10,11]. For example, a method was recently described to infiltrate solution-processable sulfide solid electrolytes into slurry-casted porous electrodes, typically employed in commercial lithium-ion batteries in combination with a liquid electrolyte [12]. Unfortunately, the development of ASSBs with sulfide solid electrolytes is hindered by their low (electro-)chemical stability and sensitivity to moisture which causes the evolution of toxic H_2S [13,14]. In addition, sulfide solid electrolytes often do not form favorable passivating films at voltages close to 0 V *vs.* Na/Na^+ or Li/Li^+ [15–17].

Meanwhile, *closo*-borates and related *closo*-carbaborates have

* Corresponding author.
** Corresponding author.
E-mail addresses: arndt.remhof@empa.ch (A. Remhof), yoonsjung@hanyang.ac.kr (Y.S. Jung).
[1] These authors contributed equally.

https://doi.org/10.1016/j.ensm.2019.11.027
Received 29 July 2019; Received in revised form 12 November 2019; Accepted 22 November 2019
Available online 27 November 2019

emerged as a promising alternative class of solid electrolytes [18–27]. They can achieve high lithium- and sodium-ion conductivities (on the order of several mS/cm) and exhibit a wide electrochemical stability window, including stability towards lithium and sodium metal anodes, high thermal and chemical stability, and stability in air (though they tend to absorb water, but can be dried easily before subsequent processing) [23,25,28–32]. They are also lighter (e.g., density of 1.17 g cm^{-3} for $Na_4(B_{12}H_{12})(B_{10}H_{10})$) than alternative solid electrolytes such as sulfides (e.g., 1.86 g cm^{-3} for Li_6PS_5Cl) and oxides (e.g., 5.01 g cm^{-3} for $Li_7La_3Zr_2O_{12}$), which may translate into a higher gravimetric energy density for batteries using *closo*-borate electrolytes. Similarly to sulfides, *closo*-borate materials are also highly deformable [28,33,34]. Thanks to this property, stable cycling of a 3 V all-solid-state battery with a sodium metal anode and a cathode fabricated by stacking and pressing of dry powders of $NaCrO_2$ (NCO) cathode material and $Na_4(B_{12}H_{12})(B_{10}H_{10})$ (NBH) *closo*-borate electrolyte was recently demonstrated [35].

Here we report the infiltration and crystallization of *closo*-borate electrolytes directly in the open porosity of slurry-casted electrodes. Thus, our electrolyte infiltration and crystallization process can be integrated into today's cell production lines after the electrode coating step substituting the electrolyte filling step thereby facilitating adoption of all-solid-state battery technology at scale. Critical for enabling this method, we show that the solution-processed $Na_4(B_{12}H_{12})(B_{10}H_{10})$ crystallizes in its highly conductive face-centered cubic (*fcc*) phase (1 mS cm^{-1} at 25 °C) using the appropriate solvent, isopropanol. The infiltration method is demonstrated for porous $NaCrO_2$ cathodes and porous Sn metal anodes for ASSBs cycling at room temperature with outstanding stability and rate capability.

2. Results and discussion

Fig. 1 illustrates the fabrication protocol used to obtain the solid-electrolyte-infiltrated electrodes. Slurry-casted electrodes consisting of $NaCrO_2$ or Sn active material powders, polyvinylidene fluoride (PVDF) binder, and conductive carbon additives (Super P) are prepared and infiltrated with $Na_4(B_{12}H_{12})(B_{10}H_{10})$ using isopropanol as a solvent. By dipping the as-prepared porous electrodes in a homogeneous isopropanol solution containing an equimolar ratio of $Na_2B_{12}H_{12}$ and $Na_2B_{10}H_{10}$ (100 mg mL^{-1}), the solution infiltrates the continuous porous network of the electrodes. After evaporation of the solvent and heat treatment at 180 °C the highly conductive $Na_4(B_{12}H_{12})(B_{10}H_{10})$ then crystallizes throughout the porous structure of the electrode. In contrast to the conventional mechano-chemical-based synthetic protocol for the preparation of *closo*-borate electrolytes [23,36], $Na_4(B_{12}H_{12})(B_{10}H_{10})$ is derived directly from its precursors *via* the solution process. The resulting solution-processed $Na_4(B_{12}H_{12})(B_{10}H_{10})$ possesses a high ionic conductivity of 1 mS cm^{-1} at room temperature, comparable to the values for samples obtained by mechano-chemical synthesis reported earlier (see Fig. S1) [23]. This is in contrast to sulfide solid electrolytes which tend to show lower conductivity after exposure to a solvent [11].

Assuming the electrolyte crystallizes only inside the porous network of the electrode (electrode porosity near 80% after casting and drying, see Table S1), we expect an electrolyte mass fraction of about 8 wt% for a $NaCrO_2$ electrode with a composition of 95:2:3 (active material to binder to carbon ratio, see Supporting Information for calculation details). The measured electrolyte mass loadings relative to the combined mass of active material, binder, and carbon after drying were about 15–17 wt% for the 97:1:2 and 95:2:3 compositions, respectively, suggesting that some electrolyte was also coated outside the porous network of the electrode. A top view SEM image and the corresponding boron energy dispersive X-ray spectroscopy (EDXS) elemental map shows an even distribution of the solid electrolyte over the surface of the $Na_4(B_{12}H_{12})(B_{10}H_{10})$-infiltrated $NaCrO_2$ electrode (Fig. S2), which confirms that the surface of the porous electrodes is also coated with $Na_4(B_{12}H_{12})(B_{10}H_{10})$, causing the difference between the measured mass loading and that expected based on the porosity of the electrode. Robust mechanical contact with the active material is formed by subsequent uniaxial cold pressing at 350 MPa also minimizing the remaining porosity. As seen in a cross-sectional scanning electron microscopy (SEM) image after pressing at 350 MPa, the infiltrated electrode appears dense throughout its thickness. The remaining porosity was estimated to be around 30%–38% based on the measured thickness and the weight of the pressed electrodes (details in the Supporting Information, Table S1). Further elaboration on the protocol, such as the control of solution concentration, downsizing $NaCrO_2$ particles, and hot pressing, may help to further decrease the porosity [12].

Fig. 2a compares the X-ray diffraction (XRD) patterns of the $NaCrO_2$ electrode before and after electrolyte infiltration, showing no alteration of the $NaCrO_2$ material. Another reflection at 2θ ~15° may be associated with the *fcc* lattice of the highly conducting $Na_4(B_{12}H_{12})(B_{10}H_{10})$ phase present in the infiltrated electrode. To confirm this, we separately crystallized $Na_4(B_{12}H_{12})(B_{10}H_{10})$ out of a solution of $Na_2B_{12}H_{12}$ and $Na_2B_{10}H_{10}$ in isopropanol, not in the electrode pores, but in a glass flask (see experimental methods for details). XRD patterns in Fig. 2b show that identical reflections are visible for the electrolyte powder obtained from solution or from a mechano-chemical synthesis employed previously [23].

Both routes thus yield $Na_4(B_{12}H_{12})(B_{10}H_{10})$ in the same *fcc* structure. In particular, the main reflection at 15° corresponds to the one seen in the infiltrated electrode in Fig. 2a. Note that when using methanol as a solvent as in a previous study [35], *fcc* $Na_4(B_{12}H_{12})(B_{10}H_{10})$ is not formed and the phases of $Na_2B_{12}H_{12}$ and $Na_2B_{10}H_{10}$ crystallize separately from solution (see Fig. S3). We also performed infrared spectroscopy, which is especially sensitive to the B-H vibrations. Fig. 2c copares the infrared spectra for the infiltrated electrode with the ones of pure $NaCrO_2$ and $Na_4(B_{12}H_{12})(B_{10}H_{10})$ powders. The same B-H stretching modes at 2400–2500 cm^{-1} and bending modes 600–1200 cm^{-1}, characteristic of the $B_{12}H_{12}^{2-}$ and $B_{10}H_{10}^{2-}$ anions, are visible in both pure $Na_4(B_{12}H_{12})(B_{10}H_{10})$ and in the infiltrated electrode. It confirms that the anions remain intact after the solution process. $NaCrO_2$ remains also unaffected by the

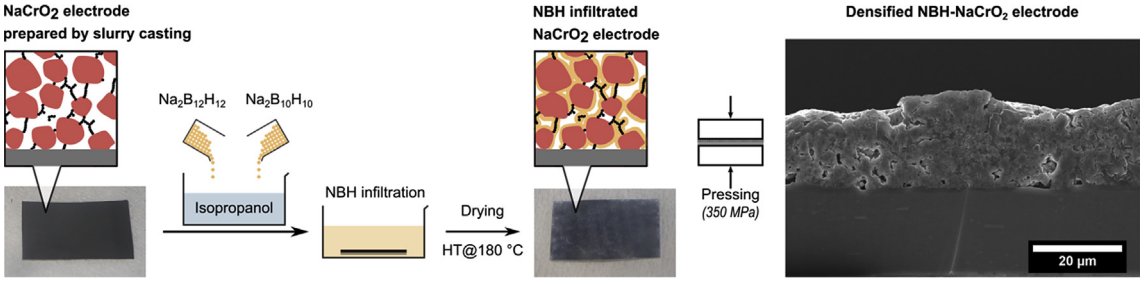

Fig. 1. Schematic diagram illustrating the fabrication of $NaCrO_2$ electrodes infiltrated with the $Na_4(B_{12}H_{12})(B_{10}H_{10})$ solid electrolyte by solution processing. Photographs of the electrodes prepared by slurry casting and their corresponding schematic cross-sectional microstructures before and after infiltration are also shown. Polymeric binders (PVDF) are not shown in the schematics for simplicity. A cross-sectional SEM image of the densified $Na_4(B_{12}H_{12})(B_{10}H_{10})$-infiltrated $NaCrO_2$ electrode is also shown.

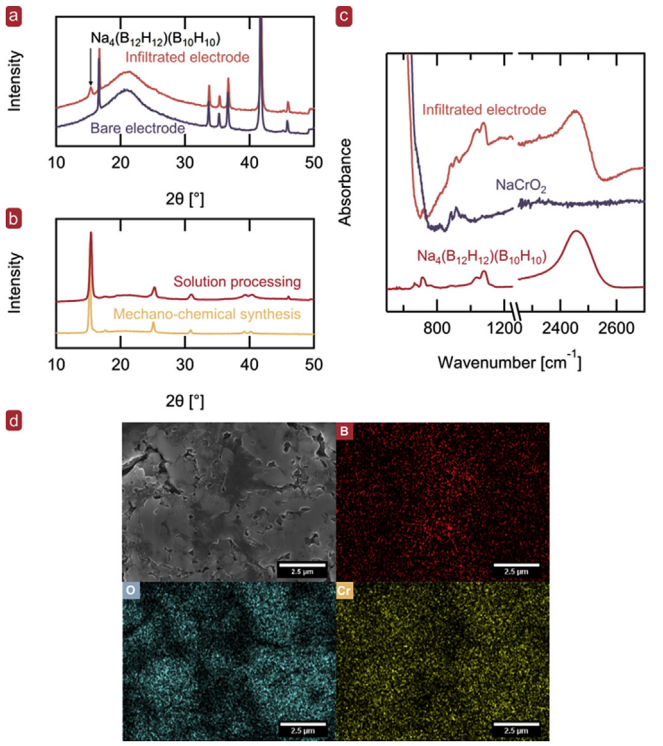

Fig. 2. Characterization of a $NaCrO_2$ electrode infiltrated with $Na_4(B_{12}H_{12})(B_{10}H_{10})$ by solution processing. (a) XRD patterns for a $NaCrO_2$ casted electrode before and after infiltration with $Na_4(B_{12}H_{12})(B_{10}H_{10})$. (b) XRD patterns of $Na_4(B_{12}H_{12})(B_{10}H_{10})$ prepared from an isopropanol solution compared to the previously reported mechano-chemical synthesis. [23] (c) Infrared absorption spectra of pure $Na_4(B_{12}H_{12})(B_{10}H_{10})$, $NaCrO_2$ powders, and a $Na_4(B_{12}H_{12})(B_{10}H_{10})$ infiltrated $NaCrO_2$ electrode. (d) Local cross-sectional SEM image and its corresponding EDXS elemental maps for an infiltrated electrode.

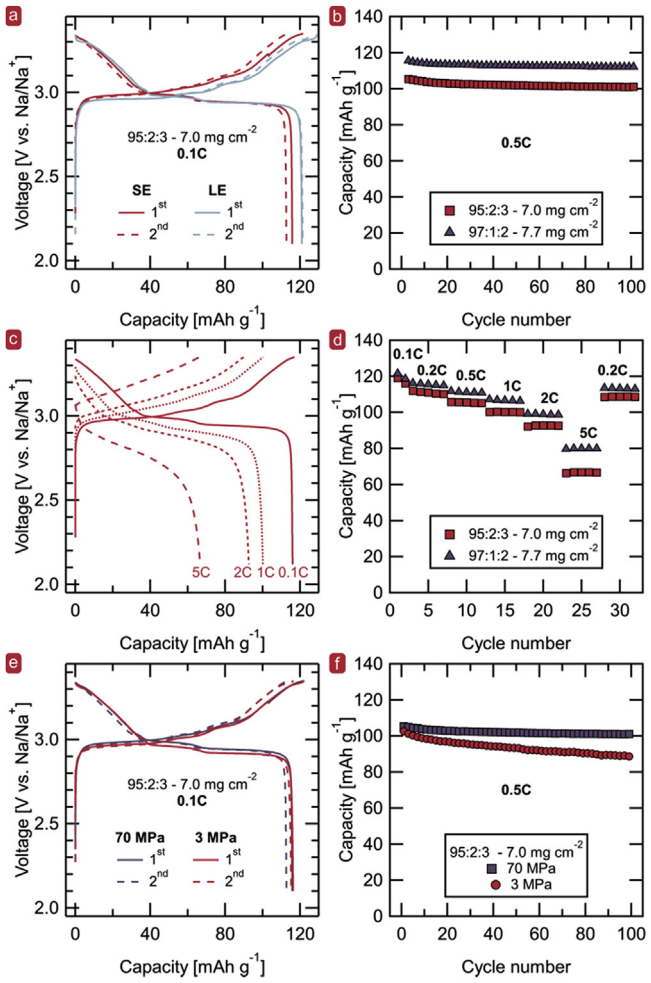

Fig. 3. Electrochemical characterization of solid-state $NaCrO_2$|$Na_4(B_{12}H_{12})(B_{10}H_{10})$|Na-Sn half cells at 30 °C. (a) Charge/discharge voltage profiles for the first two cycles of a all-solid-state $NaCrO_2$|$Na_4(B_{12}H_{12})(B_{10}H_{10})$|Na-Sn half cell at 0.1C compared to a $NaCrO_2$|1 M $NaClO_4$ in PC|Na organic liquid-electrolyte-based cell. (b) Electrochemical cycling stability upon discharge at 0.5C for two all-solid-state cells with different electrode compositions (95:2:3 and 97:1:2), after two initial cycles at 0.1C. (c) Charge/discharge voltage profiles (second cycle) at different rates of a $NaCrO_2$|$Na_4(B_{12}H_{12})(B_{10}H_{10})$|Na-Sn cell with 95:2:3 composition. (d) Rate performance upon discharge for two all-solid-state cells with different electrode compositions (95:2:3 and 97:1:2). All-solid-state cells shown in a-d were tested with applied external pressure of 70 MPa. (e) Charge/discharge voltage profiles for the 1st, 2nd cycle of $NaCrO_2$|$Na_4(B_{12}H_{12})(B_{10}H_{10})$|Na-Sn cells at 0.1C with applied external pressures of 70 MPa and 3 MPa. (f) Electrochemical cycling stability for the same cells at 0.5C after two initial cycles at 0.1C.

exposure to isopropanol. Importantly, the B-H vibrational modes correspond to the ones of the $B_{12}H_{12}^{2-}$ and $B_{10}H_{10}^{2-}$ anions in their highest symmetry configuration, I_h and D_{4d} point group symmetries, respectively, as found previously for *fcc* $Na_4(B_{12}H_{12})(B_{10}H_{10})$ [23]. No vibrational modes characteristic of isopropanol are detected, confirming the complete removal of the solvent after drying and heat treatment. In Fig. 2d, a SEM image taken within the cross section of an infiltrated electrode, along with the corresponding EDXS maps for boron, chromium, and oxygen are shown. The images were acquired in a region close to the aluminum current collector. Boron is present across the image area, notably between the chromium and oxygen rich regions, confirming an intimate mixture of $NaCrO_2$ and $Na_4(B_{12}H_{12})(B_{10}H_{10})$ throughout the electrode porous structure. $Na_4(B_{12}H_{12})(B_{10}H_{10})$ is thus present in close contact with the $NaCrO_2$ electrode particles providing continuous ion conduction pathways.

The infiltrated $NaCrO_2$ electrodes were tested in all-solid-state half cells cycled at 30 °C using a <500-µm-thick $Na_4(B_{12}H_{12})(B_{10}H_{10})$ pellet as the solid-state separator and a Na-Sn alloy counter electrode (Na_3Sn, ~0.1 V *vs.* Na/Na^+). While the electrochemical stability of $Na_4(B_{12}H_{12})(B_{10}H_{10})$ against sodium metal was previously demonstrated [23,35], we chose to employ a Na-Sn alloy to prevent non-uniform sodium metal plating. In previous experiments this was prevented by cycling at low current densities and at an elevated temperature of 60 °C [23,35]. Fig. 3a compares the voltage-capacity curves of the first two charge/discharge cycles of the all-solid-state half cell with the infiltrated $NaCrO_2$ cathode (95:2:3) at 0.1C (0.084 mA cm^{-2}), with that of an analogous cell with a liquid organic electrolyte (1 M $NaClO_4$ in propylene carbonate). The all-solid-state cell reaches a high initial discharge capacity of ~118 mA h g^{-1}, close to that of the liquid-electrolyte cell (within weighting error of 5%). Also the coulombic efficiency reaches similar values for the all-solid-state and liquid-electrolyte cell with 95.2% and 93.7% for the first cycle, respectively. For the all-solid-state cell the coulombic efficiency improves to 99.0% already for the second cycle. Long-term cycling at 0.5C shown in Fig. 3b demonstrates excellent capacity retention of 95.6% after 100 cycles with respect to the initial discharge capacity at 0.5C. These results confirm the excellent reductive stability as previously reported for $Na_4(B_{12}H_{12})(B_{10}H_{10})$ [23]. Similar cycling results were also obtained for the second infiltrated $NaCrO_2$ electrode (97:1:2, 7.7 mg cm^{-2}) with different electrode composition as shown in Fig. 3b (higher gravimetric capacity within weighting error of 5%). The SEM cross-section of a cycled electrode shown in Fig. S4 also demonstrates that the intimate ionic contacts between electrolyte and active material are maintained upon cycling. This result is well matched with the excellent cycling stability of the $Na_4(B_{12}H_{12})(B_{10}H_{10})$-infiltrated

$NaCrO_2$ electrodes.

Fig. 3c shows the voltage-capacity characteristics for the 95:2:3 electrode at different rates, while Fig. 3d compares the rate performance of the 95:2:3 (7.0 mg cm^{-2}) and the 97:1:2 (7.7 mg cm^{-2}) electrodes. Both cells exhibit remarkable rate performance. At rates as high as 5C, both electrodes with compositions of 97:1:2 and 95:2:3 retain 67.4 and 57.5% of their capacities, respectively, compared to the capacities at 0.1C. The slightly better rate capability of the electrode with 97:1:2 is consistent with the previous result observed for $LiCoO_2$ cathodes infiltrated with sulfide-based electrolytes (Li_6PS_5Cl), and was attributed to the lower binder content improving ionic contact between the $LiCoO_2$ particles [12]. Notably, the C-rate of 5C at 30 °C corresponds to a high current density of 4.5 mA cm^{-2}. This value is 45 times greater than the value reported for this electrolyte in a symmetric sodium metal cell at 60 °C [23]. This unprecedentedly high-rate capability is attributed to the high ionic conductivity of the solution-processed electrolyte and to the intimate ionic contact.

The results presented in Fig. 3a–d were obtained with an applied external pressure of 70 MPa to reduce the impact of contact loss between the electrode particles and the electrolyte upon repeated cycling. Such external pressure is often required in all-solid-state cells [37]. However, previous cell tests with $Na_4(B_{12}H_{12})(B_{10}H_{10})$ showed that stable cycling could be achieved at lower pressure given that an intimate electrode-electrolyte contact was initially formed by *e.g.* solvent impregnation of the electrolyte [35]. We thus performed additional electrochemical cycling at a reduced pressure of ~3 MPa applied by a spring. Fig. 3e shows that the two cells measured at 70 MPa and 3 MPa, respectively, behave very similarly during the first two cycles at 0.1 C, independent of the applied pressure, confirming our previous observation. Still, long-term cycling at 0.5C shown in Fig. 3f reveals that capacity fading after 100 cycles is more pronounced at 3 MPa resulting in capacity retention of 85.9% with respect to the initial discharge capacity at 0.5C, compared to 95.6% at 70 MPa. Note that *closo*-borates have favorable mechanical properties, notably a low bulk modulus on the order of 10–20 GPa, to accommodate volume changes of the electrodes upon cycling [28,33,34]. In addition, $NaCrO_2$ is known for its low volume change (<0.5%) upon cycling which may reduce the effect of external pressure on cycling stability [37].

To fabricate rocking-chair all-solid-state full cells, the solid-electrolyte infiltration method was also applied to the preparation of porous composite tin metal anodes (Sn, 10 μm). Sn was chosen for its high theoretical sodiation capacity of 847 mA h g^{-1}, low average discharge voltage, and its ductility [38]. The first two charge-discharge profiles for the solid electrolyte infiltrated Sn anode obtained in a Sn|Na-Sn half cell at 0.1C are shown in Fig. 4a. A coulombic efficiency of 84.3% is observed for the first cycle at 0.1C, improving to 97.0% for the second cycle. The discharge capacity then reaches 634 mA h g^{-1}. The Sn|Na-Sn half cell was further cycled at 0.2C, and retained 92.1% of its initial discharge capacity at 0.2C after 50 cycles (Fig. 4b).

A full cell was then built combining an infiltrated $NaCrO_2$ (97:1:2, 5.6 mg cm^{-2}) cathode with an infiltrated Sn (90:5:5, 1.2 mg cm^{-2}) anode. Based on the result of Sn|Na-Sn half cells, the Sn anode in the full cell was balanced with an excess capacity of 20% with respect to the cathode capacity (areal capacity ratio of negative to positive electrodes (np ratio) of 1.20), to minimize the risk of sodium metal plating [39]. The first two charge/discharge cycles at 0.1C (based on the cathode capacity) are shown in Fig. 4c. The cell exhibits a discharge capacity around 110 mA h g_{NCO}^{-1} *i.e.* a specific energy density of 282 W h kg_{NCO}^{-1} based on the cathode active materials weight only, and 222 W h kg^{-1} considering the total anode and cathode weights (including carbon and binder but excluding electrolyte and current collectors). The initial coulombic efficiency reaches 72.2%, as it is limited by the coulombic efficiency of the Sn anode, and climbs to 95.8% in the second cycle. The energy efficiency reaches 84.9% for the second cycle. Rate tests in Fig. S5a show that the full cell retains about 34% of its discharge capacity at 1C (constant charge of 0.1C) with respect to the initial discharge capacity at 0.1C. This poorer

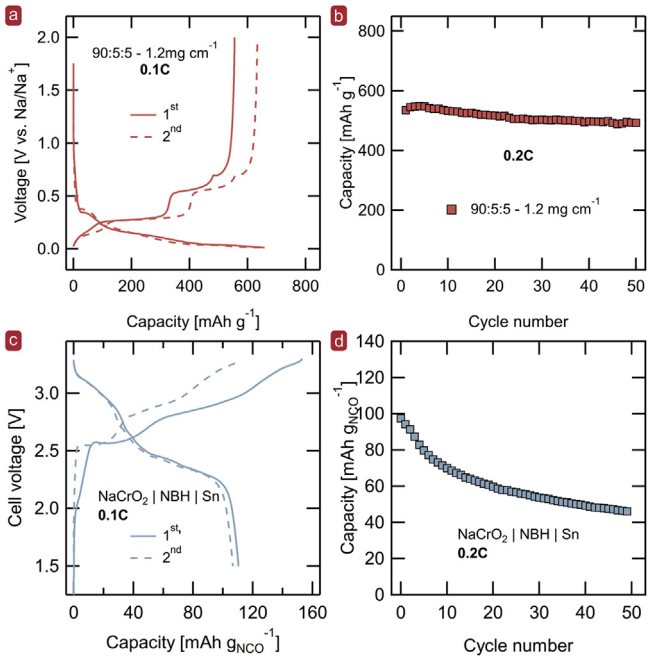

Fig. 4. Electrochemical performance of a Sn|$Na_4(B_{12}H_{12})(B_{10}H_{10})$|Na-Sn half cell and a $NaCrO_2$|$Na_4(B_{12}H_{12})(B_{10}H_{10})$|Sn full cell at 30 °C with an applied external pressure of 70 MPa. (a) Charge/discharge voltage profiles for the first two cycles of a Sn|$Na_4(B_{12}H_{12})(B_{10}H_{10})$|Na-Sn half cell at 0.1C. (b) Electrochemical cycling stability for the same cell at 0.2C after two initial cycles at 0.1C (c) Charge/discharge voltage profiles for the first two cycles of a $NaCrO_2$|$Na_4(B_{12}H_{12})(B_{10}H_{10})$|Sn full cell at 0.1C. (d) Electrochemical cycling stability for the same cell at 0.2C after two initial cycles at 0.1C.

rate capability compared to that of $NaCrO_2$ half cells is the result of the poor kinetics of sodium insertion and disinsertion in Sn as shown in the half cell rate test in Fig. S5b.

During long-term cycling at 0.2C shown in Fig. 4d, the cell shows significant capacity fading, particularly during the first ten cycles where the coulombic efficiency remains below 98%. The fading is less pronounced upon further cycling as the coulombic efficiency slowly increases to values above 99%. Ultimately, the cell retains 47.4% of its initial discharge capacity at 0.2C after 50 cycles. The comparison of coulombic efficiencies of the $NaCrO_2$ and Sn half cells in Fig. S6a shows that Sn cycles with a slower increase in coulombic efficiency and likely drives the fading of the full cell. To support this hypothesis, we cycled an additional full cell with a reduced cut-off voltage of 3.15 V shown in Fig. S6b. Because the ratio of areal capacity between anode and cathode in the full cell is 1.2, the lowering of the cut-off mainly affects the maximum potential of the cathode. We observe that a reduction of the cutoff potential does not alleviate fading of the full cell thereby confirming the role of the Sn anode in the full cell fading, in contrast to a fading caused by oxidation at higher voltages.

We further investigated the fading mechanism in an all-solid-state full cell with a three-electrode configuration to monitor the behavior of $NaCrO_2$ and Sn separately [40]. The three-electrode measurement shown in Fig. 5a confirms that the fading is caused by the poorer cyclability of the Sn anode. We observe a significant change of the voltage profile particularly during sodium insertion in Sn. However, the absence of an overpotential build-up, notably visible upon sodium removal (gray dashed lines), rules out the formation of a highly resistive interphase layer. The poor cyclability is more likely related to the large morphology and compositional change of Sn upon cycling [41]. The $NaCrO_2$ cycling behavior is then only affected as a response to the loss of Na ions at the anode. We observe that only the first plateau of the charge/discharge cycle of $NaCrO_2$ is affected during the initial cycles as illustrated by the black dashed arrow in Fig. 5b. The high voltage electrochemical activity

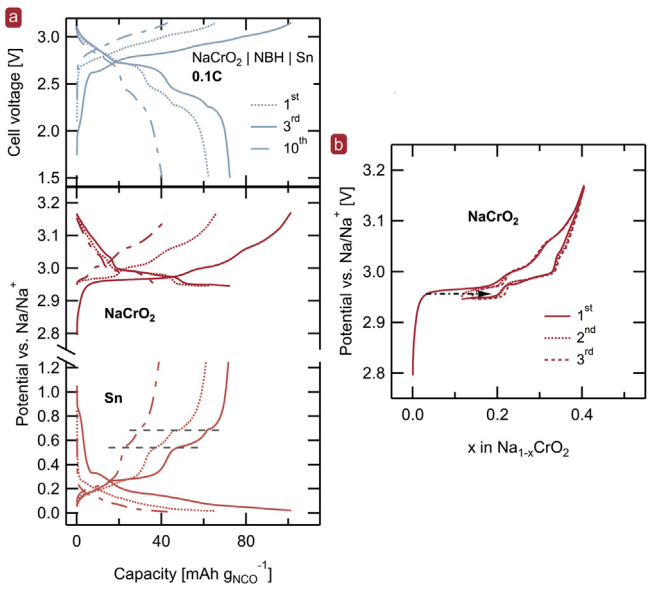

Fig. 5. (a) Charge-discharge profiles at selected cycles of a $NaCrO_2$|$Na_4(B_{12}H_{12})(B_{10}H_{10})$|Sn full cell with a three-electrode configuration cycled at 0.1C and 30 °C, along with the corresponding profiles of the separated electrodes vs. a Na/Na^+ reference electrode. The gray dashed are here to highlight the absence of overpotential build-up (b) Effect of sodium loss on the compositional cycling range of the $NaCrO_2$ cathode. The black dashed arrow highlights the change of the compositional range during cycling of $NaCrO_2$.

remains nearly unaffected. Thus, because of sodium loss on the anode side, $NaCrO_2$ cycles within a more restricted range of sodium content.

The significant difference in cycling stability observed between half cells and full cells shows the importance and difficulty of electrode balancing, a point that has rarely been discussed for all-solid-state batteries [40]. Recently, this aspect was also emphasized for lithium metal batteries which often use a largely oversized lithium metal anode which masks the loss of active lithium during cycling and leads to artificially long cycle life [42]. Generally, the underlying mechanism for the stable or unstable cycling of ASSBs has various origins, linked to both the electrochemical and mechanical stability of the electrode-electrolyte interfaces [43]. With balanced electrodes the lack of an alkali ion reservoir accentuates the fading mechanisms. In our case, the main mechanism for the capacity fading is attributed to the poor kinetics and internal stresses caused by the large volume expansion of the Sn anode upon sodium insertion, similarly to what was observed for Si in all-solid-state lithium-ion batteries [44].

3. Conclusion

In conclusion, our work demonstrates the particularly attractive combination of properties exhibited by *closo*-borate-based electrolytes, notably $Na_4(B_{12}H_{12})(B_{10}H_{10})$. It can be crystallized directly from solution into its highly conductive phase and thereby easily processed to infiltrate porous composite $NaCrO_2$ cathodes and Sn metal anodes fabricated according to established slurry-based protocols. Compared to a previous study where only a coating layer was formed onto the cathode particles by a solvent impregnation [35], the direct infiltration of crystalline $Na_4(B_{12}H_{12})(B_{10}H_{10})$ into porous electrodes, demonstrated for both cathode and anode materials, represents a significant step forward in terms of device integration. All-solid-state half cells prepared with the infiltrated electrodes can be cycled at room temperature and at high current densities up to 4.5 mA cm^{-2}, due to the high ionic conductivity of the solution processed electrolyte and the intimate ionic contacts. The remarkable cycling stability of half cells with $Na_4(B_{12}H_{12})(B_{10}H_{10})$ owes to the excellent reductive stability of $Na_4(B_{12}H_{12})(B_{10}H_{10})$.

Meanwhile, challenges remain to be solved to increase the cell voltage towards 4 V, e.g., by increasing the oxidative stability of *closo*-borate electrolytes, by developing protective cathode coatings or by the use of multiple solid electrolyte materials in a single cell. Further work is also required to understand and mitigate capacity fading in full cells with balanced electrodes. Compared to all-solid-state batteries built with thick electrodes fabricated by powder compaction [45], the method presented herein will facilitate the adoption of all-solid-state batteries based on *closo*-borates in industrial production requiring only minimal adaption of the existing fab infrastructure thereby minimizing the investment risk [8, 12].

4. Materials and methods

4.1. Materials synthesis

$Na_2B_{12}H_{12}$ and $Na_2B_{10}H_{10}$ were purchased from Katchem. $Na_2B_{12}H_{12}$ was used as received, while $Na_2B_{10}H_{10}$ was first dried under vacuum ($<10^{-3}$ mbar) at 180 °C for 6 h. For a typical 1 g batch of $Na_4(B_{12}H_{12})(B_{10}H_{10})$, 533.6 mg $Na_2B_{12}H_{12}$ and 466.4 mg $Na_2B_{10}H_{10}$ were dissolved in 20 mL anhydrous isopropanol (Sigma Aldrich). The excess solvent was first removed with a rotary evaporator. The sample was then further dried on a Schlenk line ($<10^{-3}$ mbar) at 60 °C. The obtained powder was finally heat treated at 180 °C for 4 h to yield $Na_4(B_{12}H_{12})(B_{10}H_{10})$ which was stored and handled in an argon filled glovebox. $NaCrO_2$ was synthesized according to a previously reported method [46]. Cr_2O_3 (Sigma-Aldrich) and Na_2CO_3 (Sigma-Aldrich) were mixed in a mortar for 15 min. The resulting powder was then pelletized and heat treated under argon atmosphere at 900 °C for 5 h. After the heat treatment the sample was left to cool down naturally in argon and transferred to an argon filled glovebox. The heat treated pellets were finally ground and sieved to a particle size <100 μm. The Na-Sn alloy, in a 3 to 1 M ratio, was prepared by grinding ~367.5 mg of Na with 632.5 mg of Sn with mortar and pestle in an argon filled glovebox until a dark gray powder was obtained.

4.2. Materials characterization

IR spectra were acquired on Bruker Alpha FT-IR spectrometer mounted with an ATR set-up. The spectra were measured under argon atmosphere between 400 and 4000 cm^{-1} with a resolution of 1 cm^{-1}. For XRD measurements, the $Na_4(B_{12}H_{12})(B_{10}H_{10})$ powders and infiltrated $NaCrO_2$ electrodes were covered with Be window and mounted on a MiniFlex600 diffractometer (Rigaku Corp.). Cross sections of electrodes were prepared by polishing at 4 kV for 5 h using Ar ion beam (JEOL, IB-19510CP). The SEM images and EDXS elemental maps of infiltrated $NaCrO_2$ electrodes were obtained using a JSM-7619FPlus (JEOL).

4.3. Electrode preparation

Porous composite electrodes were prepared by casting a slurry consisting of active material powder, PVDF binder (KF1100, Kureah Inc.), conductive carbon additives (Super P), and N-methyl-2-pyrrolidone (NMP) solvent on an aluminum current collector, followed by drying at 120 °C in vacuum. $NaCrO_2$ cathodes with compositions of 95:2:3 and 97:1:2 (active material to binder to carbon ratio) and Sn metal (Sigma-Aldrich, 10 μm, 99%) anodes with composition 90:5:5 were made. The as-prepared electrodes were cut in smaller pieces and dipped for 10 min in a solution containing an equimolar ratio of $Na_2B_{12}H_{12}$ and $Na_2B_{10}H_{10}$ dissolved in isopropanol at a concentration of 100 mg mL^{-1}. After dipping for 10 min, the electrodes were left to dry overnight on a flat substrate in ambient glovebox conditions. Excess solvent was finally removed by heating the electrodes to 80 °C in argon, followed by heating to 180 °C for 4 h in vacuum to crystallize the $Na_4(B_{12}H_{12})(B_{10}H_{10})$ electrolyte. We note that because $NaCrO_2$ is sensitive to humidity, cathodes were entirely prepared inside an argon filled glovebox while Sn metal anodes could be

prepared in air before being transferred to the glovebox for the solid electrolyte infiltration process. In addition, the infiltration process requires evaluating the electrode mass loading prior to the electrolyte infiltration. Generally, the mass loading of four punched 12 mm electrode was evaluated and an average was taken as the mass loading of the entire casted electrode. This may lead to some imprecision as stated in the main text but we restricted our analysis to cells with an initial discharge capacity within ±5% of the theoretical.

4.4. Cell assembly and testing

All-solid-state $NaCrO_2$ or Sn/NBH/Na-Sn half cells were prepared by the following procedure. The $Na_4(B_{12}H_{12})(B_{10}H_{10})$ powders were cold-pressed at 70 MPa, forming a solid-electrolyte layer. The infiltrated $NaCrO_2$ or Sn electrodes and Na-Sn were put on the both side of solid-electrolyte layer. Finally, assembled cells were pressed at 350 MPa in polyether ether ketone (PEEK) mold with Ti metal as current collector. The galvanostatic charge-discharge tests for half cells were carried out in the voltage ranges of 2.10–3.35 V (*vs.* Na/Na^+) for $NaCrO_2$ and 0.01–2.00 V (*vs.* Na/Na^+) for Sn electrodes at 30 °C. For all-solid-state full cells, infiltrated $NaCrO_2$ and Sn electrodes were put on the both side of a $Na_4(B_{12}H_{12})(B_{10}H_{10})$ solid electrolyte layer, followed by pressing at 350 MPa and cycled between 1.5 and 3.3 V at 30 °C. All-solid-state three-electrode cells were fabricated by the same procedure in our previous report [38]. The $NaCrO_2/Na_4(B_{12}H_{12})(B_{10}H_{10})$/Sn full cells were pressed at 350 MPa. Then, additional SE layers (50 mg of $Na_4(B_{12}H_{12})(B_{10}H_{10})$) and Na metal as the reference electrode were put on top of the $NaCrO_2$ electrode, followed by pressing at 70 MPa. A small piece of Al current collector of the $NaCrO_2$ electrode was carefully peeled off in order to ionically connect the Na metal and the $NaCrO_2$ electrode through the $Na_4(B_{12}H_{12})(B_{10}H_{10})$ layer. The resulting three-electrode cell configuration is a $Na/Na_4(B_{12}H_{12})(B_{10}H_{10})/NaCrO_2/Na_4(B_{12}H_{12})(B_{10}H_{10})$/Sn. The liquid-electrolyte cells using Na metal counter electrodes were tested using 2032-type coin cells. The 1 M $NaClO_4$ in propylene carbonate (PC) was used as the liquid electrolyte and glass fiber sheet was used as the separator.

Supporting Information

Calculation details for the electrode porosity and estimated solid electrolyte mass loading. Conductivity of the solution processed $Na_4(B_{12}H_{12})(B_{10}H_{10})$. SEM micrographs from an as-prepared and cycled cell, rate performance tests of a Sn/NBH/Na-Sn half-cell and an NCO/NBH/Sn full cell, Coulombic efficiencies and cycling stabilities.

Data availability statement

The raw and processed data required to reproduce these findings cannot be shared at this time as the data also forms part of an ongoing study.

Notes

The authors declare no competing financial interest.

Declaration of competing interest

The authors declare no competing interests.

Acknowledgment

L.D., R.M., H.H, A.R, and C. B. thank the Swiss National Science Foundation (SNSF) for financial support for the Sinergia project 'Novel ionic conductors' under contract number CRSII2_160749/1. This work was further partially supported by InnoSuisse through funding for the Swiss Competence Center for Energy Research (SCCER) Heat and Electricity Storage under contract number 1155-002545. L.D. thanks the Korean National Research Foundation (NRF) for a young researcher's exchange grant. Y.S.J. was supported by the Technology Development Program to Solve Climate Changes and by Basic Science Research Program through the National Research Foundation of Korea (NRF) funded by the Ministry of Science, ICT & Future Planning (Nos. NRF-2017M1A2A2044501 and NRF-2018R1A2B6004996).

Appendix A. Supplementary data

Supplementary data to this article can be found online at https://doi.org/10.1016/j.ensm.2019.11.027.

References

[1] J. Janek, W.G. Zeier, A solid future for battery development, Nat. Energy. 1 (2016) 16141, https://doi.org/10.1038/nenergy.2016.141.
[2] K.H. Park, Q. Bai, D.H. Kim, D.Y. Oh, Y. Zhu, Y. Mo, Y.S. Jung, Design strategies, practical considerations, and new solution processes of sulfide solid electrolytes for all-solid-state batteries, Adv. Energy Mater. 8 (2018) 1800035, https://doi.org/10.1002/aenm.201800035.
[3] C. Vaalma, D. Buchholz, M. Weil, S. Passerini, A cost and resource analysis of sodium-ion batteries, Nat. Rev. Mater. 3 (2018) 18013, https://doi.org/10.1038/natrevmats.2018.13.
[4] A. Manthiram, X. Yu, S. Wang, Lithium battery chemistries enabled by solid-state electrolytes, Nat. Rev. Mater. 2 (2017) 1–16, https://doi.org/10.1038/natrevmats.2016.103.
[5] Z. Zhang, Y. Shao, B. Lotsch, Y.-S. Hu, H. Li, J. Janek, L.F. Nazar, C.-W. Nan, J. Maier, M. Armand, L. Chen, New horizons for inorganic solid state ion conductors, Energy Environ. Sci. (2018) 1945–1976, https://doi.org/10.1039/C8EE01053F.
[6] C. Zhou, S. Bag, V. Thangadurai, Engineering materials for progressive all-solid-state Na batteries, ACS Energy Lett 3 (2018) 2181–2198, https://doi.org/10.1021/acsenergylett.8b00948.
[7] Y. Lu, L. Li, Q. Zhang, Z. Niu, J. Chen, Electrolyte and interface engineering for solid-state sodium batteries, Joule 2 (2018) 1747–1770, https://doi.org/10.1016/J.JOULE.2018.07.028.
[8] J. Schnell, T. Günther, T. Knoche, C. Vieider, L. Köhler, A. Just, M. Keller, S. Passerini, G. Reinhart, All-solid-state lithium-ion and lithium metal batteries – paving the way to large-scale production, J. Power Sources 382 (2018) 160–175, https://doi.org/10.1016/j.jpowsour.2018.02.062.
[9] D.Y. Oh, Y.J. Nam, K.H. Park, S.H. Jung, K.T. Kim, A.R. Ha, Y.S. Jung, Slurry-fabricable Li^+ -conductive polymeric binders for practical all-solid-state lithium-ion batteries enabled by solvate ionic liquids, Adv. Energy Mater (2019) 1802927, https://doi.org/10.1002/aenm.201802927.
[10] S. Ohta, J. Seki, Y. Yagi, Y. Kihira, T. Tani, T. Asaoka, Co-sinterable lithium garnet-type oxide electrolyte with cathode for all-solid-state lithium ion battery, J. Power Sources 265 (2014) 40–44, https://doi.org/10.1016/J.JPOWSOUR.2014.04.065.
[11] A. Banerjee, K.H. Park, J.W. Heo, Y.J. Nam, C.K. Moon, S.M. Oh, S.-T. Hong, Y.S. Jung, Na_3SbS_4 : a solution processable sodium superionic conductor for all-solid-state sodium-ion batteries, Angew. Chem. Int. Ed. 55 (2016) 9634–9638, https://doi.org/10.1002/anie.201604158.
[12] D.H. Kim, D.Y. Oh, K.H. Park, Y.E. Choi, Y.J. Nam, H.A. Lee, S.-M. Lee, Y.S. Jung, Infiltration of solution-processable solid electrolytes into conventional Li-Ion-Battery electrodes for all-solid-state Li-ion batteries, Nano Lett. 17 (2017) 3013–3020, https://doi.org/10.1021/acs.nanolett.7b00330.
[13] W.D. Richards, L.J. Miara, Y. Wang, J.C. Kim, G. Ceder, Interface stability in solid-state batteries, Chem. Mater. 28 (2016) 266–273, https://doi.org/10.1021/acs.chemmater.5b04082.
[14] H. Muramatsu, A. Hayashi, T. Ohtomo, S. Hama, M. Tatsumisago, Structural change of Li2S–P2S5 sulfide solid electrolytes in the atmosphere, Solid State Ion. 182 (2011) 116–119, https://doi.org/10.1016/J.SSI.2010.10.013.
[15] S. Wenzel, T. Leichtweiss, D.A. Weber, J. Sann, W.G. Zeier, J. Janek, Interfacial reactivity benchmarking of the sodium ion conductors Na_3PS_4 and sodium β-alumina for protected sodium metal anodes and sodium all-solid-state batteries, ACS Appl. Mater. Interfaces 8 (2016) 28216–28224, https://doi.org/10.1021/acsami.6b10119.
[16] C.K. Moon, H.-J. Lee, K.H. Park, H. Kwak, J.W. Heo, K. Choi, H. Yang, M.-S. Kim, S.-T. Hong, J.H. Lee, Y.S. Jung, Vacancy-driven Na^+Superionic conduction in new Ca-doped Na_3PS_4 for all-solid-state Na-ion batteries, ACS Energy Lett 3 (2018) 2504–2512, https://doi.org/10.1021/acsenergylett.8b01479.
[17] S. Wenzel, S. Randau, T. Leichtweiß, D.A. Weber, J. Sann, W.G. Zeier, J. Janek, Direct observation of the interfacial instability of the fast ionic conductor $Li_{10}GeP_2S_{12}$ at the lithium metal anode, Chem. Mater. 28 (2016) 2400–2407, https://doi.org/10.1021/acs.chemmater.6b00610.
[18] T.J. Udovic, M. Matsuo, W.S. Tang, H. Wu, V. Stavila, A.V. Soloninin, R.V. Skoryunov, O.A. Babanova, A.V. Skripov, J.J. Rush, A. Unemoto, H. Takamura, S. Orimo, Exceptional superionic conductivity in disordered sodium decahydro-closo-decaborate, Adv. Mater. 26 (2014) 7622–7626, https://doi.org/10.1002/adma.201403157.

[19] T.J. Udovic, M. Matsuo, A. Unemoto, N. Verdal, V. Stavila, A.V. Skripov, J.J. Rush, H. Takamura, S. Orimo, Sodium superionic conduction in $Na_2B_{12}H_{12}$, Chem. Commun. 50 (2014) 3750, https://doi.org/10.1039/c3cc49805k.
[20] W.S. Tang, A. Unemoto, W. Zhou, V. Stavila, M. Matsuo, H. Wu, S. Orimo, T.J. Udovic, Unparalleled lithium and sodium superionic conduction in solid electrolytes with large monovalent cage-like anions, Energy Environ. Sci. 8 (2015) 3637–3645, https://doi.org/10.1039/C5EE02941D.
[21] W.S. Tang, M. Matsuo, H. Wu, V. Stavila, W. Zhou, A.A. Talin, A.V. Soloninin, R.V. Skoryunov, O.A. Babanova, A.V. Skripov, A. Unemoto, S.-I. Orimo, T.J. Udovic, Liquid-Like ionic conduction in solid lithium and sodium monocarba- closo -decaborates near or at room temperature, Adv. Energy Mater. 6 (2016) 1502237, https://doi.org/10.1002/aenm.201502237.
[22] W.S. Tang, K. Yoshida, A.V. Soloninin, R.V. Skoryunov, O.A. Babanova, A.V. Skripov, M. Dimitrievska, V. Stavila, S. Orimo, T.J. Udovic, Stabilizing superionic-conducting structures via mixed-anion solid solutions of monocarba-closo -borate salts, ACS Energy Lett 1 (2016) 659–664, https://doi.org/10.1021/acsenergylett.6b00310.
[23] L. Duchêne, R.-S. Kühnel, D. Rentsch, A. Remhof, H. Hagemann, C. Battaglia, A highly stable sodium solid-state electrolyte based on a dodeca/deca-borate equimolar mixture, Chem. Commun. 53 (2017) 4195–4198, https://doi.org/10.1039/C7CC00794A.
[24] M. Brighi, F. Murgia, Z. Łodziana, P. Schouwink, A. Wołczyk, R. Černý, A mixed anion hydroborate/carba-hydroborate as a room temperature Na-ion solid electrolyte, J. Power Sources 404 (2018) 7–12, https://doi.org/10.1016/j.jpowsour.2018.09.085.
[25] S. Kim, H. Oguchi, N. Toyama, T. Sato, S. Takagi, T. Otomo, D. Arunkumar, N. Kuwata, J. Kawamura, S. Orimo, A complex hydride lithium superionic conductor for high-energy-density all-solid-state lithium metal batteries, Nat. Commun. 10 (2019) 1081, https://doi.org/10.1038/s41467-019-09061-9.
[26] L. Duchêne, A. Remhof, H. Hagemann, C. Battaglia, Status and prospects of hydroborate electrolytes for all-solid-state batteries, Energy Storage Mater (2019), https://doi.org/10.1016/j.ensm.2019.08.032.
[27] F. Murgia, M. Brighi, R. Černý, Room-temperature-operating Na solid-state battery with complex hydride as electrolyte, Electrochem. Commun. 106 (2019) 106534, https://doi.org/10.1016/J.ELECOM.2019.106534.
[28] Z. Lu, F. Ciucci, Metal borohydrides as electrolytes for solid-state Li, Na, Mg, and Ca batteries: a first-principles study, Chem. Mater. 29 (2017) 9308–9319, https://doi.org/10.1021/acs.chemmater.7b03284.
[29] L. He, H.W. Li, E. Akiba, Thermal decomposition of anhydrous alkali metal dodecaborates $M_2B_{12}H_{12}$ (M = Li, Na, K), Energies 8 (2015) 12429–12438, https://doi.org/10.3390/en81112326.
[30] E.L. Muetterties, J.H. Balthis, Y.T. Chia, W.H. Knoth, H.C. Miller, Chemistry of boranes. VIII. Salts and acids of $B_{10}H_{10}^{2}$ and $B_{12}H_{12}^{2}$, Inorg. Chem. 3 (1964) 444–451, https://doi.org/10.1021/ic50013a030.
[31] M.P. Pitt, M. Paskevicius, D.H. Brown, D.A. Sheppard, C.E. Buckley, Thermal stability of $Li_2B_{12}H_{12}$ and its role in the decomposition of $LiBH_4$, J. Am. Chem. Soc. 135 (2013) 6930–6941, https://doi.org/10.1021/ja400131b.
[32] L. Duchêne, S. Lunghammer, T. Burankova, W.-C. Liao, J.P. Embs, C. Copéret, H.M.R. Wilkening, A. Remhof, H. Hagemann, C. Battaglia, Ionic conduction mechanism in the $Na_2(B_{12}H_{12})_{0.5}(B_{10}H_{10})_{0.5}$ closo-borate solid-state electrolyte: interplay of disorder and ion–ion interactions, Chem. Mater. 31 (2019) 3449–3460, https://doi.org/10.1021/acs.chemmater.9b00610.
[33] R. Moury, Z. Łodziana, A. Remhof, L. Duchêne, E. Roedern, A. Gigante, H. Hagemann, Pressure-induced phase transitions in $Na_2B_{12}H_{12}$, structural investigation on a candidate for solid-state electrolyte, Acta Crystallogr. Sect. B Struct. Sci. Cryst. Eng. Mater. 75 (2019) 406–413, https://doi.org/10.1107/S2052520619004670.
[34] H. Chen, T. Hong, First-principles investigation of the mechanical and thermodynamic properties of the metal-borohydrides as electrolytes for solid-state batteries, J. Electrochem. Soc. 166 (2019) A493–A500, https://doi.org/10.1149/2.0071904jes.
[35] L. Duchêne, R.-S. Kühnel, E. Stilp, E. Cuervo Reyes, A. Remhof, H. Hagemann, C. Battaglia, A stable 3 V all-solid-state sodium–ion battery based on a closo -borate electrolyte, Energy Environ. Sci. 10 (2017) 2609–2615, https://doi.org/10.1039/C7EE02420G.
[36] W.S. Tang, M. Matsuo, H. Wu, V. Stavila, A. Unemoto, S. Orimo, T.J. Udovic, Stabilizing lithium and sodium fast-ion conduction in solid polyhedral-borate salts at device-relevant temperatures, Energy Storage Mater 4 (2016) 79–83, https://doi.org/10.1016/j.ensm.2016.03.004.
[37] D.M. Piper, T.A. Yersak, S.-H. Lee, Effect of compressive stress on electrochemical performance of silicon anodes, J. Electrochem. Soc. 160 (2013) A77–A81, https://doi.org/10.1149/2.064301jes.
[38] L.D. Ellis, T.D. Hatchard, M.N. Obrovac, Reversible insertion of sodium in tin, J. Electrochem. Soc. 159 (2012) A1801–A1805, https://doi.org/10.1149/2.037211jes.
[39] C.-S. Kim, K.M. Jeong, K. Kim, C.-W. Yi, Effects of capacity ratios between anode and cathode on electrochemical properties for lithium polymer batteries, Electrochim. Acta 155 (2015) 431–436, https://doi.org/10.1016/J.ELECTACTA.2014.12.005.
[40] Y.J. Nam, K.H. Park, D.Y. Oh, W.H. An, Y.S. Jung, Diagnosis of failure modes for all-solid-state Li-ion batteries enabled by three-electrode cells, J. Mater. Chem. A. 6 (2018) 14867–14875, https://doi.org/10.1039/C8TA03450H.
[41] Z. Li, J. Ding, D. Mitlin, Tin and tin compounds for sodium ion battery anodes: phase transformations and performance, Acc. Chem. Res. 48 (2015) 1657–1665, https://doi.org/10.1021/acs.accounts.5b00114.
[42] J. Liu, Z. Bao, Y. Cui, E.J. Dufek, J.B. Goodenough, P. Khalifah, Q. Li, B.Y. Liaw, P. Liu, A. Manthiram, Y.S. Meng, V.R. Subramanian, M.F. Toney, V.V. Viswanathan, M.S. Whittingham, J. Xiao, W. Xu, J. Yang, X.-Q. Yang, J.-G. Zhang, Pathways for practical high-energy long-cycling lithium metal batteries, Nat. Energy. 4 (2019) 180–186, https://doi.org/10.1038/s41560-019-0338-x.
[43] R. Koerver, I. Aygün, T. Leichtweiß, C. Dietrich, W. Zhang, J.O. Binder, P. Hartmann, W.G. Zeier, J. Janek, Capacity fade in solid-state batteries: interphase formation and chemomechanical processes in nickel-rich layered oxide cathodes and lithium thiophosphate solid electrolytes, Chem. Mater. 29 (2017) 5574–5582, https://doi.org/10.1021/acs.chemmater.7b00931.
[44] D.H. Kim, H.A. Lee, Y.B. Song, J.W. Park, S.-M. Lee, Y.S. Jung, Sheet-type Li_6PS_5Cl-infiltrated Si anodes fabricated by solution process for all-solid-state lithium-ion batteries, J. Power Sources 426 (2019) 143–150, https://doi.org/10.1016/j.jpowsour.2019.04.028.
[45] Y. Kato, S. Shiotani, K. Morita, K. Suzuki, M. Hirayama, R. Kanno, All-solid-state batteries with thick electrode configurations, J. Phys. Chem. Lett. 9 (2018) 607–613, https://doi.org/10.1021/acs.jpclett.7b02880.
[46] S. Komaba, C. Takei, T. Nakayama, A. Ogata, N. Yabuuchi, Electrochemical intercalation activity of layered $NaCrO_2$ vs. $LiCrO_2$, Electrochem. Commun. 12 (2010) 355–358, https://doi.org/10.1016/j.elecom.2009.12.033.